Electro-mechanical validation of a resonant MEMS mirror with PZT actuation and PZR sensing

G.Mendicino[a*], M.Merli[a], R.Carminati[a], N.Boni[a], A.Opreni[b] and A. Frangi[b]
[a]STMicroelectronics, AMS Group, Via Tolomeo 1, Cornaredo, Milan, Italy 20010
[b]Department of Civil and Environmental Engineering, Politecnico di Milano, Milano, Italy

ABSTRACT

MEMS mirrors are used in projection systems based on Laser Beam Scanning LBS and hence they are involved in applications as Augmented Reality Headset and LiDAR. Characterization of the electro-mechanical behavior of MEMS structures plays an important role in the following control strategy definition and system integration.
A mono-axial resonant PZT actuated MEMS mirror is addressed and the characteristics of the mechanical structure is investigated by measuring the frequency response of the functional and the main spurious vibrational modes. In addition, a dedicated analysis on the nonlinear behavior is performed Calibration stations with camera sensors are used for optical and electrical analyses while vibrometric and stroboscopic measurement techniques are employed for detecting micrometric movements of the structure.
A piezoresistive sensor with Wheatstone bridge configuration is built on board of the MEMS mirror for tracking mirror position during actuation. The combined effects of the functional and spurious modes on the sensor frequency response are evaluated and compared with the MEMS mirror model.
In this work, a full characterization on the electro-mechanical parameters of a resonant mono-axial PZT actuated MEMS mirror is presented and a detailed comparison between collected data and model prediction is reported.

Keywords: MEMS Mirror, Laser Beam Scanning, Piezoelectric, LiDAR, AR/VR

1. INTRODUCTION

MEMS mirrors for Laser Beam Scanning (LBS) represent a growing technology. AR/VR and LiDAR are the two main areas in which this class of devices are gathering industrial interest. Several LBS-based products are already available on the market like Microsoft Hololens 2 [1] (augmented reality) and Intel Real Sense [2] (LiDAR).

Different technology platforms can be used for building MEMS actuators in order to address several application requirements: electrostatic, magnetic and piezoelectric technologies. The experimental activity reported in this work has been done on a low frequency (2 kHz) resonant mirror with PZT actuation. This device with 3mm mirror diameter and 60° optical Field of View (FoV) at 15 V has ideal specifications for LIDAR applications [3]. This technology uses a modulated laser for measuring distances in its FoV. The time of flight between emitted and received light is used for measuring distances. A schematic representation of the working principle is reported in Figure 1. According to the application requirements, it possible to measure in short range (~10 m) or long range (~200 m).

*gianluca.mendicino@st.com

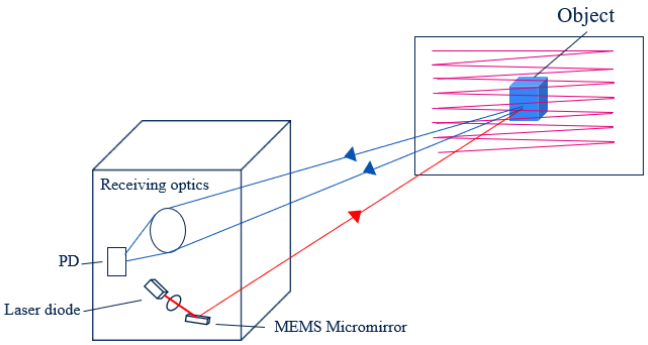

Figure 1: Schematic representation of a scanning LIDAR system.

The manuscript is organized as follows. A detailed device description together with the modelling approach is reported in Section 2. The analysis introduces a study of system nonlinearities to improve the standard linear approach. Those models are widely used for control systems development in order to predict the electromechanical response of the mirror.
The advanced laboratory instruments used in the experimental phase are presented in Section 3. In Section 4 experimental techniques for a complete electromechanical MEMS mirror modelling are reported. The comparison between the experiment and the model is reported in Section 5.
In Section 5 a detailed analysis of the MEMS mirror power consumption is analyzed. This information is used during the electronics design phase to reduce the energy cost of the MEMS mirror.

2. MEMS DESCRIPTION

The device under investigation is a mono-axial resonant MEMS mirror developed and fabricated by STMicroelectronics using PεTRA technology platform [4], ST proprietary technology dedicated to PZT thin film MEMS actuators.

Figure 2(b) shows the schematic layout of the device, highlighting its main features [5]. The mirror mass, located at the center of the device, is characterized by a high reflectance area of 3 mm diameter for the MEMS mirror primary function of light deflection. Two torsional springs connecting the suspended mass to the anchoring points allow the mirror to rotate around the x-axis. Four trapezoidal beams, hereafter labelled actuators, realized in thin-film PZT as active layer, are linked to the reflective area through folded actuator springs. Mirror rotation sensing is performed through a piezoresistive sensor in Wheatstone's bridge configuration located at the base of the torsional springs.

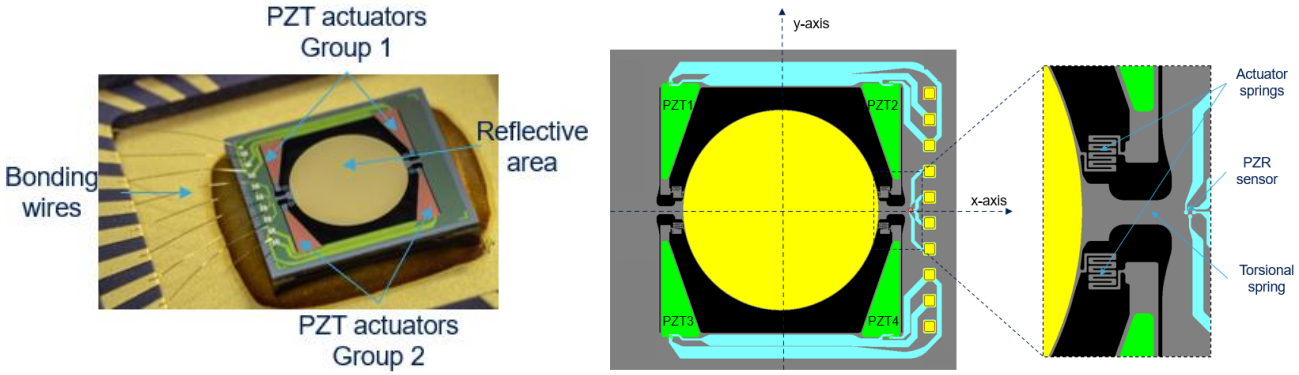

(a) (b)

Figure 2: (a) Wire bonded MEMS mirror; (b) Layout schematic

In Figure 2(a) a picture of a wire-bonded sample is reported. PZT patches used for actuation are grouped in two sets: PZT1 and PZT2 form set1 and PZT3 and PZT4 form set2. Actuation at resonance can be performed by means of only one PZT set or altogether with appropriate waveforms. The PZT patches are driven with fully positive voltage signals to prevent

accelerated aging of piezoelectric properties, hence reducing the durability of the device. Figure 3 shows an example of mirror actuation and sense signals, i.e. the square wave actuation of both PZT groups and the resulting mirror angle and PZR sensor signals. A 180° phase shift between the PZT set1 and set2 is needed for creating a non-null modal force acting on the mirror when both actuator sets are involved.

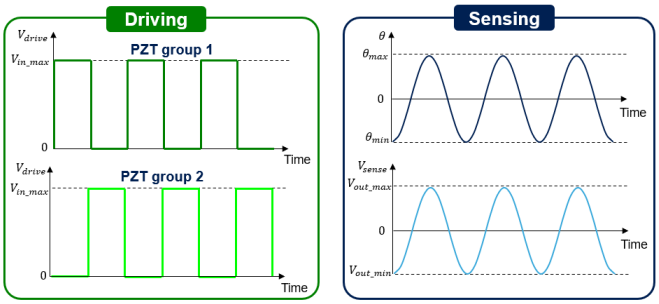

Figure 3: Actuation and sensing signals (schematic)

During operation, the device is actuated at its first resonance mode. The associated displacement field is reported in Figure 4(a): the reflective area rotates rigidly around the x-axis. In this way the incident light is reflected to the target location.
The most relevant spurious modes for the device configuration are the Z-mode (Figure 4(b)), which is a vertical translation of the reflective surface, and the actuators mode (Figure 4(c)), that corresponds to a bending motion of the actuators. Due to the displayed mechanical modes shape and PZT actuators location, these spurious modes are expected to introduce nonlinearities in the PZR sensor output signal.

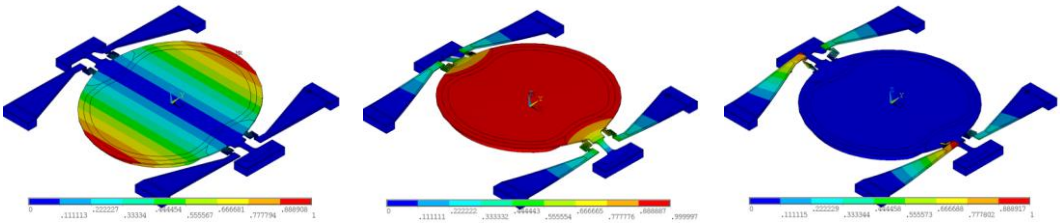

(a) (b) (c)

Figure 4 – FEM simulations, main mechanical modes: (a) Torsional mode (operational); (b) Z- mode (spurious); (c) Actuator mode (spurious)

2.1 Modelling description

2.1.1 Dynamic Model

A reduced order model based on linear modal superposition has been used for describing the MEMS mirror behavior. The schematic view reported in Figure 5 shows the main blocks of the model and the general organization of input and output parameters. The micromirror can be actuated with either one or two PZT sets. The mirror opening angle is estimated only from the response of the main torsional mode under the assumption of negligible contribution from the other modes. PZR sensor signal is calculated by summing the effects stemming from all mechanical modes that are involved in the model. The first few modes up to 25kHz were found appropriate for modeling the device considered in this work. A description of the main blocks of the model is presented in the following.

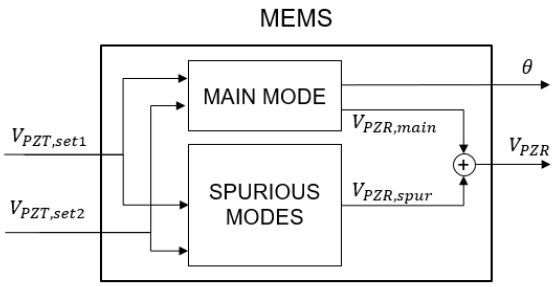

Figure 5: MEMS model schematic

MAIN MODE

The main mode is described by the coordinate θ, which represents the rotation of the reflective mirror plate. Considering the high displacements reached by the mechanical structure during device operation, its mathematical formulation includes the typical nonlinear effects found in MEMS mirrors for the damping torque $F_D(\dot{\theta}, \theta)$ as in ([6][7][8]) and the restoring action $F_k(\theta)$ as in [6]. The dynamics of the main mode is:

$$J\ddot{\theta} + F_D(\dot{\theta}, \theta) + F_k(\theta) = T_{PZT}(t) \tag{1}$$

The dissipative action is expressed as:

$$F_D(\dot{\theta}, \theta) = \frac{1}{2}\rho_{air} AF CD_{air} |\dot{\theta}| \dot{\theta} \tag{2}$$

Where ρ_{air} is the air density at reference temperature, AF accounts for the in-plane form factor geometry, $\dot{\theta}$ is the mirror angular speed and CD_{air} is the air drag coefficient expressed as a function of the Reynolds (Re) number. The latter term has been measured and experimental data results are reported in the characterization section.

The restoring action is expressed as:

$$F_k(\theta) = k_0\theta + k_2\theta^3 \tag{3}$$

The elastic torque is modeled as a 3rd order polynomial, where k_0 and k_2 are the polynomial coefficients. k_0 is calculated by Finite Element Method (FEM) modal analysis and k_2 is chosen to get a good fit with the experimental backbone curve extracted by the main mode frequency response function (FRF).

The torque created by the combined effects of the PZT actuation sets is:

$$T_{PZT} = \eta(V_0)V \tag{4}$$

Where: V is the driving voltage, V_0 is the amplitude value of V and η is the experimental piezoelectric coefficient. The last term is calculated by the FRF measurements of the main mode.

SPURIOUS MODES

The remaining mechanical modes are represented as a classical linear time invariant 2nd order mechanical system:

$$m_i\ddot{x}_i + c_i\dot{x}_i + k_i x_i = \eta_i V \qquad i = 1,2,\dots,N \tag{5}$$

Where: m_i and k_i are respectively the modal mass and stiffness. They are obtained by a FEM modal analysis. η_i, c_i, are the modal piezoelectric and damping coefficients. They are estimated by dedicated measurements reported section 4.2.

PZR SENSOR
The sensor response of each mechanical mode is described by the following relation:

$$V_{out} = \alpha_i x_i V_b \tag{6}$$

Where α_i is the modal sensor sensitivity in $[\frac{mV}{\mu mV}]$ for translational modes and $[\frac{mV}{degV}]$ for rotational modes, x_i is the reference coordinate expressed in $[\mu m]$ for translational modes or $[deg]$ for rotational modes and V_b is the bias voltage applied to the Wheatstone's bridge.

2.1.2 Power calculation

The estimation of the power required by the actuators is done through an empirical model based on the hysteretic behavior of the PZT material displayed by the polarization curve. The experimental curve collected at 15V is reported in Figure 6.

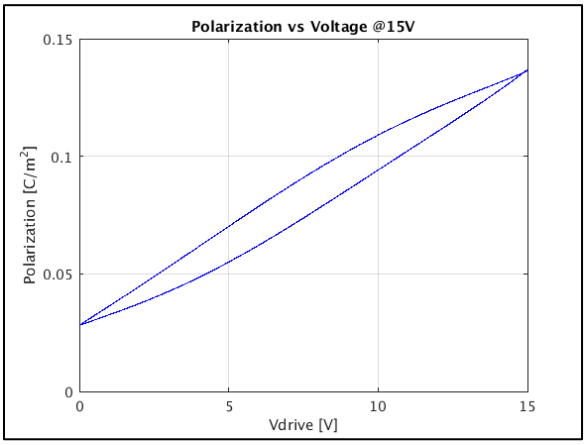

Figure 6 - Experimental polarization curve

The current flowing in and out from the capacitor upon a specific drive voltage waveform is calculated starting from the relation between charge and polarization:

$$Q(t) = A_{pzt} P\big(V(t)\big) \tag{7}$$

The current is obtained as:

$$I(t) = \frac{d\big(Q(t)\big)}{dt} = A_{pzt} \frac{d\left(P\big(V(t)\big)\right)}{dt} = A_{pzt} \frac{dP}{dV} \frac{dV}{dt} \tag{8}$$

Finally, the dissipative P_{res} and stored P_{cap} powers are:

$$P_{res} = \frac{1}{T} \int_0^T VI \, dt \tag{9}$$

$$P_{cap} = \sqrt{\left(\frac{1}{T} \int_0^T |VI| \, dt\right)^2 - P_{res}^2} \tag{10}$$

The resistive term P_{res} is a fraction of the total power, and it is dissipated. On the other hand, the capacitive term can be partially recovered by adopting dedicated solutions during the MEMS driver design phase.

3. EXPERIMENTAL ACTIVITY DESCRIPTION

In this section we report the experimental setup required to characterize the device.

3.1 Measurement Station

A measurement station has been assembled for collecting the mirror opening angle at different operating conditions. The setup is composed by a laser, a camera, a projection screen, a function generator and an oscilloscope, as reported in Figure 7. The laser crosses the projection screen through a dedicated aperture and it hits the mirror surface with normal incidence. The mirror movement deflects the laser light and it creates a line on the screen. The projected image is collected using a camera. By processing the picture, the line length is measured. The line length is the correlated to the opening angle of the device.

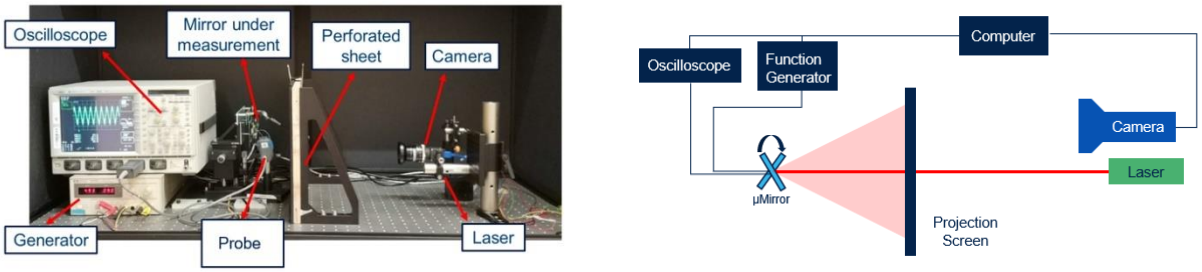

(a) (b)

Figure 7: Measurement station: (a) picture; (b) Schematic view

Another key parameter of the MEMS mirror is the PZR sensor response. A DC voltage supply and an oscilloscope are connected to the device to measure the sensor electrical properties. The time domain signal is then collected and processed to extract the main features i.e. the PZR sensor sensitivity and the FRF of sensor output. The entire measurement process is managed by a computer through a dedicated software developed by ST for this purpose.

3.2 Vibrometer

The study of the MEMS mirror mechanical structure is done using the Polytec MSA-500 Vibrometer [9], the latter reported in Figure 8a. Thanks to laser doppler techniques, this instrument measures displacement and velocity of a point on the structure. Upon definition of a dedicated mesh a dedicated mesh, Figure 8b, it is possible to measure different points on the structure. As a result, the structure motion can be reconstructed with accuracy of the order or few nanometers. As a result, it is possible to measure the motion of the structure when excited at one of its resonance modes. Some examples are reported in the next section in Figure 13.

3.3 Audio analyzer

A dedicated study of the PZR sensor response is required for a complete characterization of the device. This analysis has been done using the UPV Rohde&Schwarz audio analyzer [10]. Using this instrument, it is possible to drive the mirror with sinewaves up to 20 V amplitude at different frequencies, ranging from 20 Hz up to 80 kHz. The sensor signal can be collected with a sensitivity of the order of the micro-Volt, thanks to a low noise differential input. The signal is then processed to obtain the PZR transfer function.

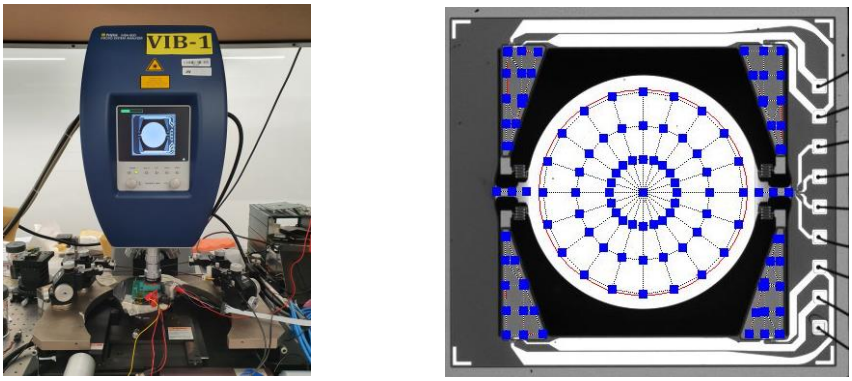

(a) (b)

Figure 8: (a) Polytec: instrument picture; (b) Meshed Lynx

4. EXPERIMENTAL RESULTS

In this section the experimental results are reported along with the model prediction.

4.1 Main mode characterization

The characterization of the MEMS mirror functional mode is mainly based on the FRF. Almost all the parameters involved in the modeling of the dynamics of the main mechanical mode can be extracted from post processing on the FRF curves at different drive voltage levels. In the following, the experimental estimation of the parameters needed to fulfill the dynamical model of the main mode are described.

4.1.1 FRFs and backbone curve

The torsional mode at 1.9 kHz has been fully characterized since it is used as functional mode. Its performances are measured using two different techniques. The automatic measurement station with a camera sensor, described in section 3.1, has been chosen for higher half mechanical opening angles up to 15°. The collected FRFs are reported in Figure 9a. The vibrometric technique, described in section 3.2, has been used to investigate the MEMS mirror performance at lower angles (less than 1° half mechanical) and the experimental findings are plotted in Figure 9b.

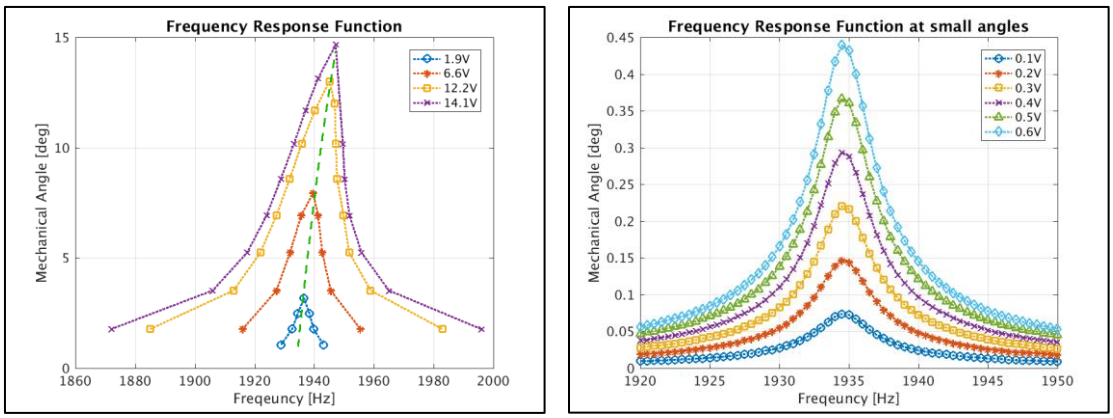

(a) (b)

Figure 9: Frequency response function at different drive voltage peaks: (a) High opening angle measurements with the automatic measurement station. The backbone curve is also highlighted in green dashed line; (b) Low opening angle measurements through vibrometric technique.

The shape of the different FRF curves highlights the nonlinear behavior of the torsionale mode. The backbone curve highlights the hardening response of the device.

4.1.2 Quality factor

The quality factor of nonlinear systems under the assumption of quadratic damping, as assumed for the device in this work, can be calculated by the following equation [11]:

$$Q = \frac{f_n}{\Delta f}\sqrt{n^2 - \frac{1}{n^2}} \tag{11}$$

Where f_n is the linear resonance frequency, Δf is the frequency difference between two points of the curve haing the same angle a and n is the ratio between a and the maximum angle a_n. Figure 10a shows how the quality factor decreases as the opening angle increases. This effect is caused by the strong influence that viscous fluid damping has on the dynamic response of the structure. Indeed, since the device operates in air, drag causes strong damping nonlinearities [7][8]. The formulation of the damping torque, described in Section 2.1.1, depends on the air drag coefficient CD_{air}.

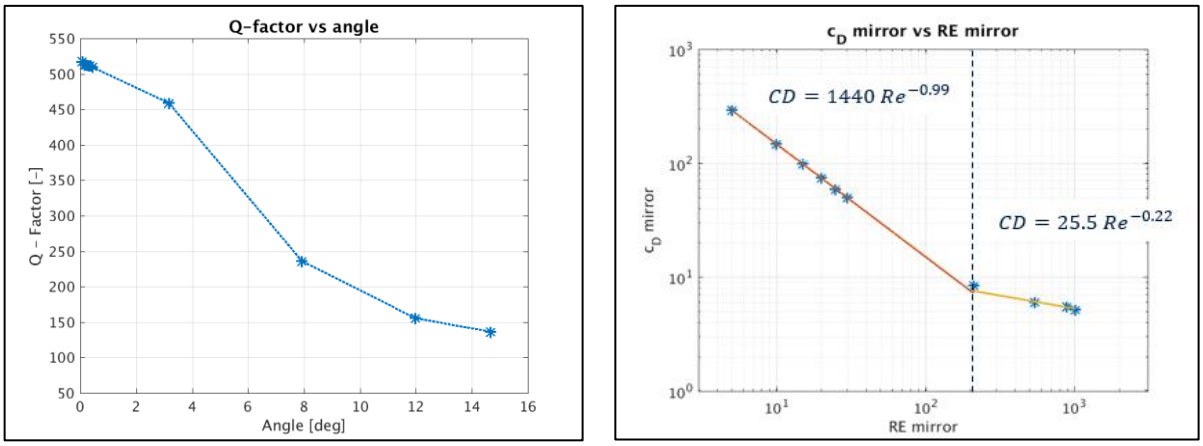

(a) (b)

Figure 10: (a) Quality Factor at different opening angles; (b) Cd versus Reynolds number

The experimental behavior of the quality factor over the entire operative range is reported in Figure 10a: the quality factor decreases starting from about 500 at very small angles to about 140 at 15°. Furthermore, the air drag coefficient CD_{air} has been calculated by the Q factor definition reported in [8] and plotted against the Re number in Figure 10b. Two main regions can be identified: at low Re(up to about 100) the CD_{air} is almost proportional to Re^{-1} reducing the influence of the scanning angle over Q, while, for higher Re values the CD_{air} tends to be less dependent on Re, hence resulting in a higher influence of opening angle on the quality factor. The experimental behavior of CD_{air} has been included into the damping torque modeling.

4.1.3 Piezoelectric coefficient η

The piezoelectric coefficient estimation can be approached from the analysis of the main mode FRF curves. At resonance, neglecting the contribution of spurious modes, the viscous torque is balanced by the equivalent torque given by the PZT actuators:

$$c\dot{\theta}_0 = \eta V_0 \tag{12}$$

By rearranging (12) and considering the relation between c and Q through $c = \frac{J\omega_0}{Q}$, it is possible to obtain the formula:

$$\eta = \frac{k_0 \theta_0}{Q\, V_0} \tag{13}$$

Where V_0 is the drive voltage amplitude, θ_0 is the amplitude opening angle, k_0 is the modal stiffenes and Q is the quality factor.

Results of (13) based on the experimental measurements θ_0 and Q at a defined V_0 values are plotted in Figure 11. The piezoelectric coefficient increases as the voltage amplitude increases, as reported in Figure 11. This results is of particular interest for MEMS mirrors since it confirms the nonlinear behavior of the PZT thin film under the electric field values requested by this class of devices.

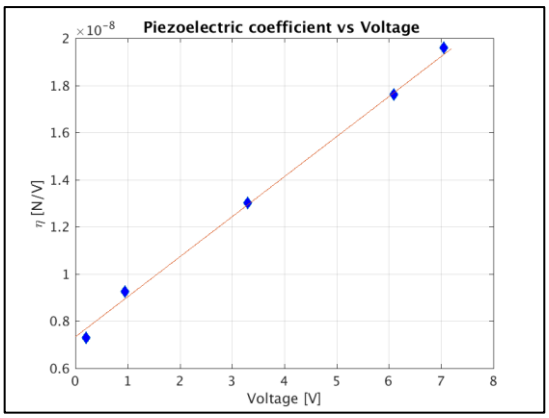

Figure 11: Main mode $\boldsymbol{\eta}$ parameter as a function of driving voltage

4.1.4 PZR sensor sensitivity $\boldsymbol{\alpha}$

The PZR sensor response of the main torsional mode has been characterized by driving the MEMS mirror at resonance with a sinwave signal involving both PZT actuator groups. The sinusoidal movement of the device is converted into an electrical signal by the PZR sensor. This signal is collected, analyzed and compared to the opening angle measured with the optical setup. As reported in Figure 12, the sensor sensitivity is the resulting slope of the linear regression of the sensor output voltage against the opening angle.

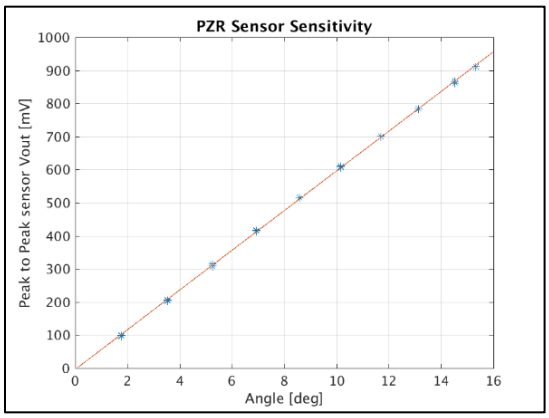

Figure 12: PZR sensor sensitivity. The line represents the linear fit of the experimental data.

The sensitivity value obtained by fitting the experimental data is 9.98mV/V/deg.

4.2 Spurious mode characterization

The mechanical response study of the system is done using a vibrometer. The definition of a complete mesh on the device enables the acquisition of the out of plane motion of the structure. By combining the motion of each single measurement point defined by the mesh it is possible to evaluate the motion the system. Vibrational modes with resonance frequency up to 30 kHz have been analyzed. In the spectrum reported in Figure 13 the first peak is the torsionale mode (main mode). The second and third peaks are two 'spurious modes', corresponding to a vertical traslation of the device and to a bending of the actuators.

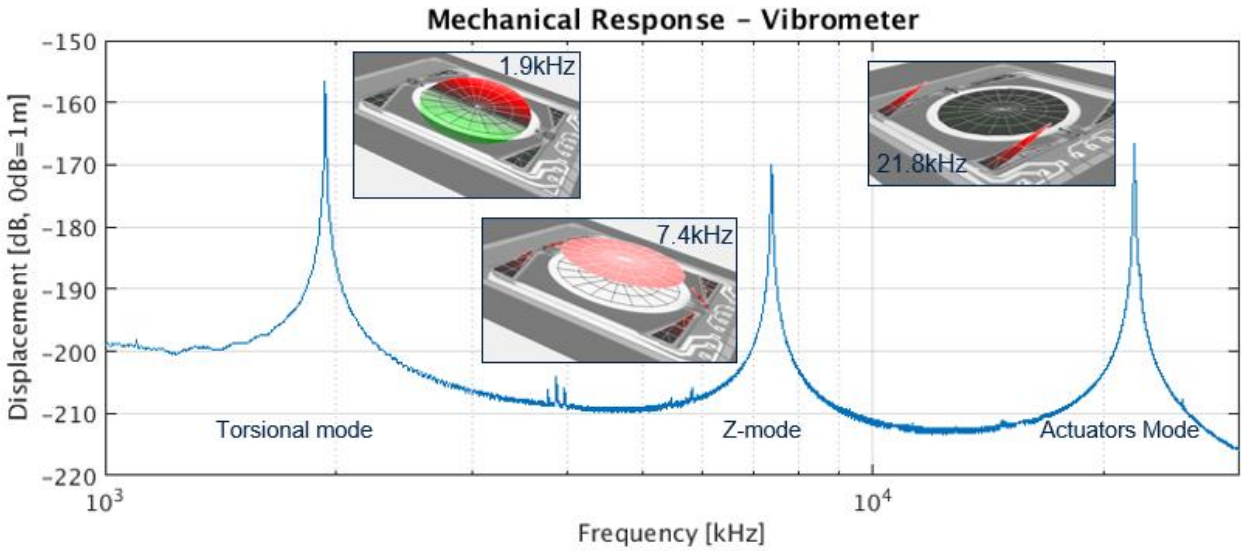

Figure 13: Mechanical response of the out of plane modes up to 30kHz. The pictures in the graph show the modal shape collected with vibrometer.

The comparison between experimental results and FEM simulation data shows a good agreement between model and experiment.

Mode	FEM [Hz]	Experimental Results [Hz]	Error [%]
Torsional [Hz]	2020	1940	4.1
Z – Displacement [Hz]	7450	7360	1.2
Actuators [Hz]	22215	21790	2.0

Table 1: Resonance frequencies: simulation vs measurements

The frequency response function of the modes plays an important role in the experimental analysis. Since spurious modes do not provide any optical feedback, the motion of the structure must be collected using vibrometric techniques. The time domain mechanical response of a relevant point of the structure is measured. In Figure 14 the meaningful points for the two spurious modes under investigation are highlighted.

The structure has been excited with a sinewave at a fixed frequency. The steady state mechanical response has been collected and analyzed and the displacement has been recorded. This measurement has been performed at different frequencies and different drive voltages. The obtained results are reported in Figure 15.

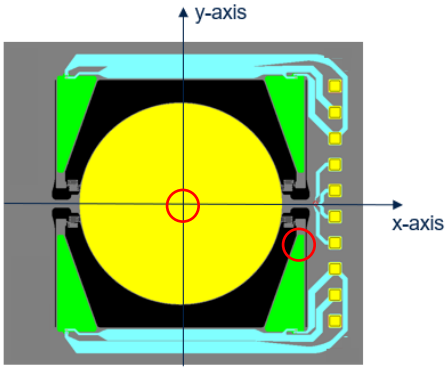

Figure 14: Measurement points for spurious mode motion detection.

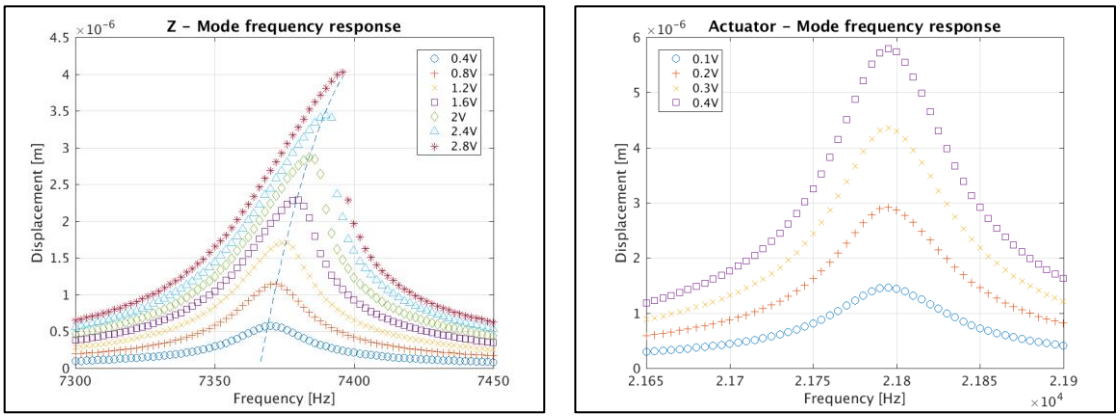

Figure 15: Spurious modes FRFs. Backbone curve in 'Z-mode' graph is reported in dashed line.

It is possible to observe a nonlinear hardening behavior for the Z-mode and a linear mechanical response for the actuator bending mode. The hardening behavior of the Z-mode is caused by the axial reaction of the torsional springs used to suspend the reflective surface. On the other hand, actuators behave as clamped-free beams, which are known for their highly linear response even at large displacements.

The PZR sensor sensitivity of the two spurious modes has been measured. The displacement of the structure together with electrical signal produced on the sensor must be collected. The displacement of the structure is measured using the Vibrometer in time domain configuration. The two sensors output are combined and amplified through a dedicated board and they are then collected using an oscilloscope. The amplitude of the movement versus the electrical signal amplitude is fitted with a linear function as reported in Figure 16.

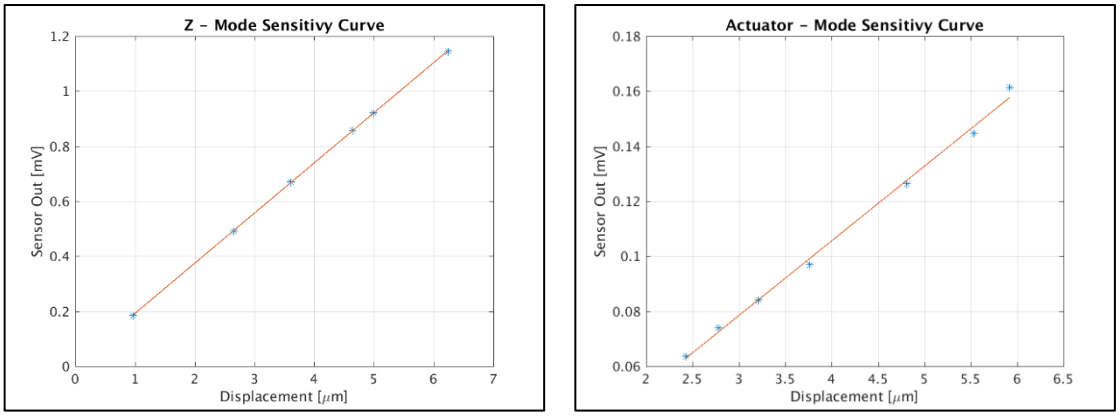

(a) (b)

Figure 16: Sensitivity curves for Z-mode (a) and actuator mode (b)

The obtained sensitivity values are reported in Table 2.

Mode	Sensitivity [mV/V/µm]
Z-mode	0.061
Actuator Mode	0.009

Table 2: Sensitivity values for spurious mode, obtained by fitting experimental data.

In order to have a complete modelling of the spurious modes the η parameter, presented in 4.2, has been extracted. The obtained values are reported in Table 3.

Mode	η [N/V]
Z-mode	$1.27 \cdot 10^{-5}$
Actuator Mode	$1.54 \cdot 10^{-1}$

Table 3: η values for Z displacement and Actuators spurious modes

5. SIMULATION AND EXPERIMENTAL RESULTS

The model scheme described in Section 2.1.1 has been integrated into the Simulink environment. Simulation results for the main mode and the PZR sensor transfer function have been compared with the measurements collected on a sample that has been fully characterized.
Furthermore, the power contributions involved in the PZT actuator excitation over a relatively wide frequency range about the main mode have been measured.

5.1 Dynamic results

MAIN MODE FRF
FRF measurement has been performed activating the MEMS mirror with fully positive sinewaves on both PZT actuator sets at different driving voltage levels covering a large half mechanical scan angle range up to about 15°. The comparison between measurements and the simulation are reported in Figure 17.

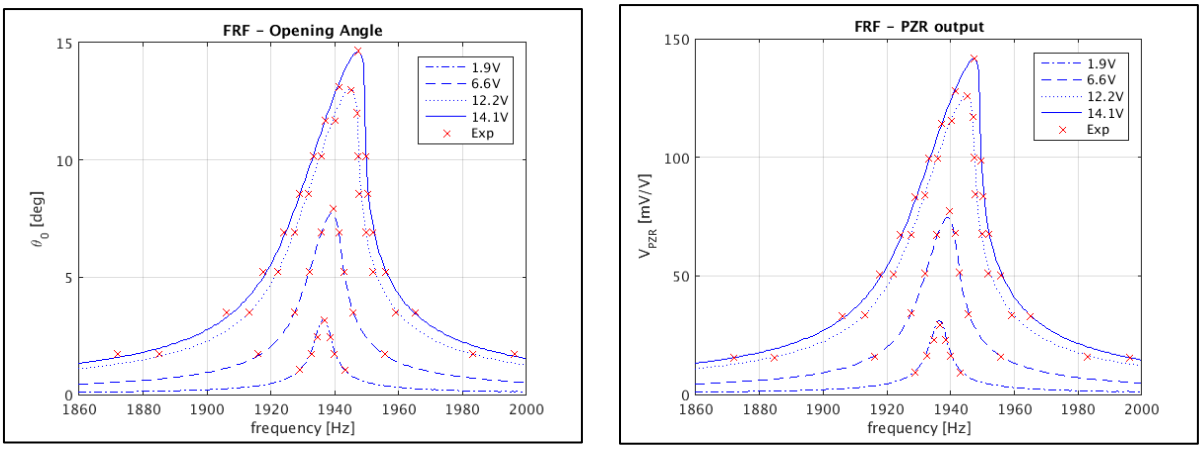

(a) (b)

Figure 17: FRF measurement at different driving voltage: (a) half mechanical opening angle; (b) PZR sensor

The model can replicate both the mechanical nonlinearity, as highlighted by the identical hardening response, and the damping dissipation that increases at higher mechanical opening angles. A good agreement can be observed over the entire explored mechanical angle range. The maximum amplitude error between model predictions and experimental observations for both the opening angle and PZR output are within the ±5% range. The biggest errors are found for lower angle curves due to a lower setup accuracy in that range.

PZR SENSOR TRANSFER FUNCTION

PZR sensor transfer function has been measured up to 25kHz. The response has been evaluated for the case in single PZT actuation set configuration. Results are reported in Figure 18.

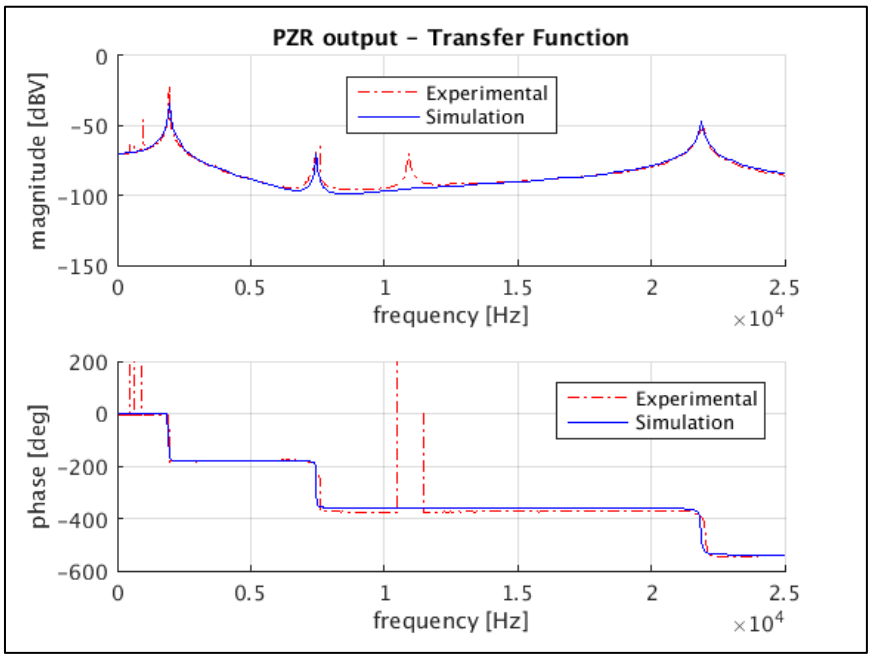

Figure 18: PZR sensor transfer function: PZT actuator set1

The obtained results show a good match with the corresponding experimental dataset. The spectrum shape and frequency location of both resonances and anti-resonances are well predicted by the model.

The additional peaks in the experimental results at ~1 kHz and ~11 kHz are related to sub-harmonic nonlinear excitation. The measurement setup adopted in this metric is not able to discriminate such a nonlinear behavior.

5.2 Power results

Power consumption measurements have been performed over a wide frequency range up to 5 kHz by actuating only one PZT actuator set with a fully positive sinewave at a voltage peak of 15 V. The corresponding polarization curve has been split into two branches: charge phase (up) and discharge phase (down). Each polarization branch has been fitted with a 5th order polynomial, as reported in Equations (14) and (15), and plotted in Figure 19.

$$P_{up} = \sum_{n=0}^{N} a_n^{(c)} V^n \tag{14}$$

$$P_{down} = \sum_{n=0}^{N} a_n^{(d)} V^n \tag{15}$$

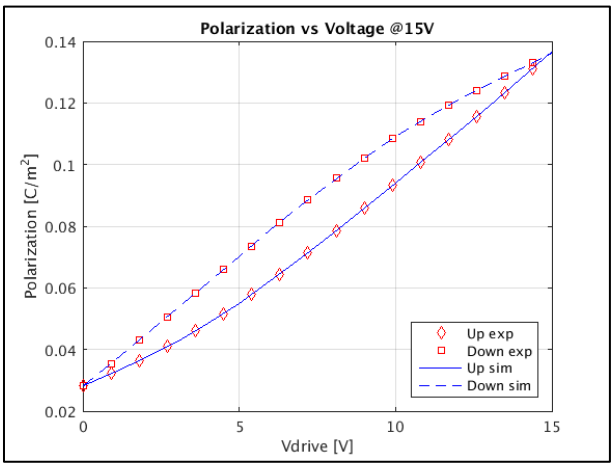

Figure 19: Polarization curve at 15V

Given a drive voltage wave form, as the one in Figure 20a, the current flowing through the capacitor is obtained as:

$$I(t) = \begin{cases} A_{pzt} \sum_{n=0}^{N} n\, a_n^{(c)} V^{n-1} \dfrac{dV}{dt} & if \ \dfrac{dV}{dt} > 0 \\ A_{pzt} \sum_{n=0}^{N} n\, a_n^{(d)} V^{n-1} \dfrac{dV}{dt} & if \ \dfrac{dV}{dt} < 0 \end{cases} \tag{16}$$

The current calculated by the presented model allows predicting the experimental data points in Figure 20b.

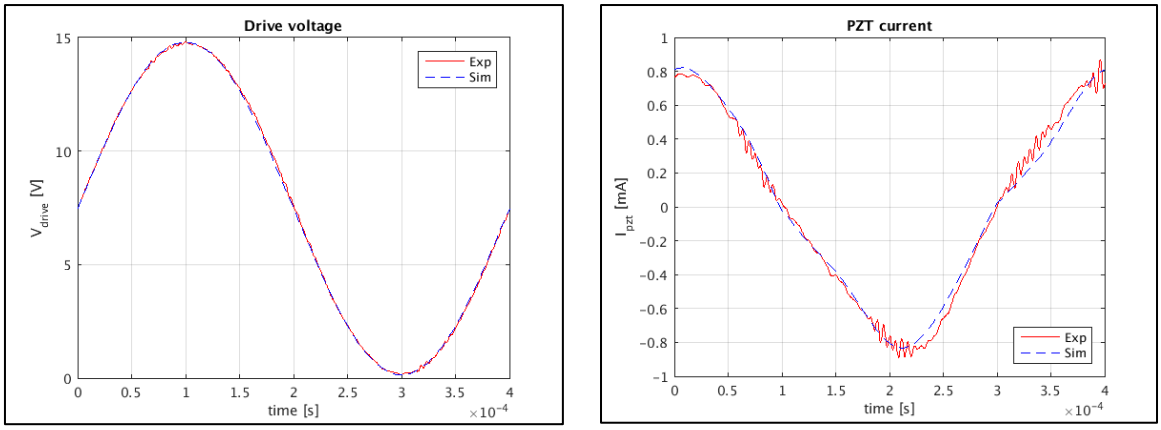

(a) (b)

Figure 20: Electrical waveform; (a)Drive voltage; (b)PZT current

Power consumption results divided into capacitive and resistive contributors are presented in Figure 21.

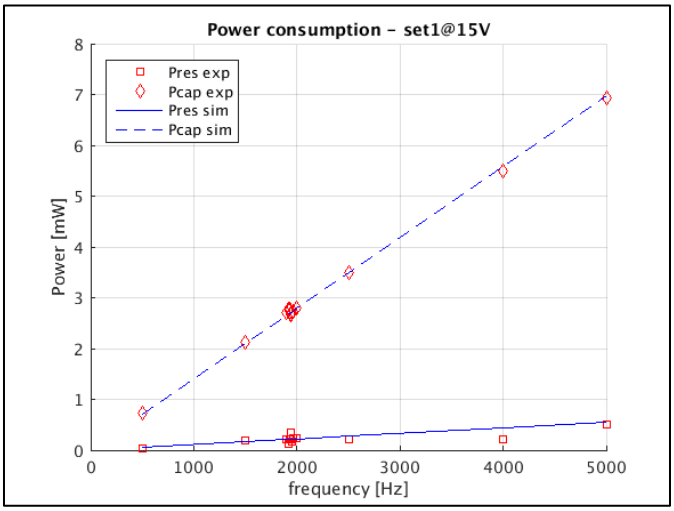

Figure 21: PZT power consumption

There is a good accordance between experimental and simulation data. The capacitive term is well fitted with a maximum error of 4.1%, while the resistive term is overestimated with a maximum error up to 26% out of resonance. The whole behavior of the power requested by the PZT is mainly related to the electrical properties displaying a linear trend with driving frequency. The additional mechanical loss source, dependent on the mirror actuation at high opening angles, is present as a local amplification in the resistive power at the resonant frequency, reaching 0.36 mW from a bottom line of 0.22 mW.

6. CONCLUSION

In the present work, a detailed analysis of the experimental techniques for MEMS mirror electromechanical modeling has been presented. The activities have been performed on a piezoelectric resonant mirror with large reflective area (7.1 mm^2) and high performances with low driving voltage, up to 60° full FOV @ 15 V. The electromechanical behavior up to 25 kHz has been deeply analyzed with focus on the nonlinear response of both main and spurious modes. A complete model has been developed showing a good agreement between experiments and simulations.

The power consumption of the MEMS mirror has been investigated. The low power consumption is highlighted by the model and confirmed by experiments, and it is less than 3 mW at 2 kHz with 0.36 mW resistive power.

Acknowledgements

The authors wish to thank the MEMS technology R&D team, working at STMicroelectronics in Agrate (Italy), for fabricating the device and all the Characterization and Application teams, working at STMicroelectronics in Castelletto (Italy), for the automated tools development.

REFERENCES

[1] Microsoft Hololens 2: https://www.microsoft.com/en-us/hololens
[2] Intel RealSense L515: https://www.intelrealsense.com/lidar-camera-l515/
[3] Wang, D.; Watkins, C.; Xie, H. MEMS Mirrors for LiDAR: A Review. *Micromachines* 2020, *11*, 456
[4] STMicroelectronics PεTRA technology platform: https://investors.st.com/news-releases/news-release-details/stmicroelectronics-and-usound-deliver-first-advanced-mems
[5] Boni, N., Carminati, R., Merli, M., inventors; STMicroelectronics S.r.l., assignee, 2020, Jun 18. Microelectromechanical device with a structure tiltable by piezoelectric actuation having improved mechanical and electrical characteristics. United States Patent Application No. 16/704,484.
[6] Frangi, A., Opreni, A., Boni, N., Fedeli, P., Carminati, R., Merli, M., Mendicino, G., "Nonlinear Response of PZT-Actuated Resonant Micromirrors", J. Microelectrom. Syst., 29(6), 1421-1430 (2020).
[7] W. O. Davis, "Nonlinear drag damping of torsional microscanners," in Proc. Transducers, 2011, pp. 1424–1427.
[8] Davis, W. "Empirical analysis of form drag damping for scanning micromirrors", Proc. SPIE 7208, (2009).
[9] Polytec MSA-500: https://www.polytec.com/int
[10] https://www.rohde-schwarz.com/us/product/upv-productstartpage_63493-7558.html?change_c=true
[11] W. O. Davis, "Measuring quality factor from a nonlinear frequency response with jump discontinuities," J. Microelectromech. Syst., vol. 20, no. 4, pp. 968–975, Aug. 2011.